

Fast prediction of the long-range structural acoustic radiation in the stratified ocean

Ruixin Nie^{a,1}, Tengjiao He^{a,1}, Jun Fan^{a,1}, Kaiqi Zhao^{a,1} and Bin Wang^{a,1}

^aKey Laboratory of Marine Intelligent Equipment and System, Ministry of Education, Shanghai Jiaotong University, shanghai, 200240, PR China

ARTICLE INFO

Keywords:

Underwater radiated noise
Wave superposition method
Normal-mode model

ABSTRACT


In this study, we propose an efficient method for predicting three-dimensional acoustic radiation from arbitrary structures immersed in a shallow-water waveguide. By incorporating the finite element method (FEM) and the wave superposition method (WSM), the detailed acoustic radiation from the vibrating structure in the near field is calculated by numerically evaluating the source strength integral that represents the Helmholtz exterior problem. Transitioning to the far-field region, where the structural acoustic radiation is characterized by the source directionality, an analytical, normal-mode expression for the source-strength integral is derived, representing the structural acoustic radiation as a sum over propagating eigenmodes, with the modal excitation determined by the directionality of the acoustic radiation mode. This represents a significant improvement in numerical efficiency by reducing computational complexity, especially for high-frequency and long-range predictions. The critical distance distinguishing the near-field and far-field regions is discussed in detail, determined by the horizontal wavenumber and structure size. Numerical simulations demonstrate the effectiveness of the proposed method and reveal the coupling mechanism between the structural acoustic radiation and the underwater acoustic propagation. The proposed method is adaptable to optimize the passive sonar performance by achieving the real-time prediction of the structural acoustic radiation in realistic ocean-acoustic environments.

1. Introduction

Predicting acoustic radiation from vibrating structures is crucial for underwater remote sensing and target detection. This prediction is a direct tool for evaluating the passive sonar performance and structural health of underwater vehicles during the design and maintenance stages. Therefore, efficient and accurate methods for calculating the vibro-acoustics of underwater structures have received considerable attention in recent years. However, when underwater vehicles operate in shallow seas, where boundary reflections and acoustic refraction may occur, the radiated field is severely distorted and influenced by waveguide physics, which involves complicated coupling mechanisms between structural acoustic radiation and underwater acoustic propagation. Therefore, the modeling of structural acoustic radiation in shallow water typically involves multiphysics disciplines, which complicates the modeling process and increases the difficulty of achieving fast and accurate solutions.

Historically, both analytical (Li et al., 2014; Guo et al., 2017; Zhao et al., 2020; Kha et al., 2024) and numerical methods have been developed to calculate the acoustic radiation from an arbitrary radiator submerged in fluids. Analytical methods generally handle the simplest situations in which regular structures and infinite or semi-infinite fluids without inhomogeneities are considered. However, numerical methods combine numerical analysis to solve the vibro-acoustics of the fluid-loaded structure and an exterior solver to calculate the Helmholtz exterior problem and sound propagation. The finite element method (FEM) is extremely versatile because it is fully customizable in terms of the material and geometric parameters considered in the simulations. Thus, it is a useful tool for vibro-acoustic analysis when modeling structural acoustic radiation in fluids. However, restrained by volume discretization, the computational domain of the FEM typically has several acoustic wavelengths, and the frequency of the simulation lies in the low-to-middle frequency range (Ochmann, 2004). Alternatively, an appropriate solver for the exterior Helmholtz problem can be integrated with the FEM to handle far-field radiation by discretizing only the surface of the structure instead of the entire computational domain. For instance, the Kirchhoff approximation (KA) has proven to be effective for

*Corresponding author.

 bin_wang@sjtu.edu.cn (B. Wang)

ORCID(s):

¹ Also at: School of Ocean and Civil Engineering, Shanghai Jiao Tong University, Shanghai, 200240, PR China.

calculating far-field radiation from vibrating structures at high frequencies (Freund et al., 1996). In the low-to-middle frequency region, where the validity of KA is violated, the boundary element method (BEM) has been widely applied to calculate the radiated field produced by structures submerged in an infinite fluid or ocean waveguide (Brunner et al., 2010; Jin et al., 2018). The fact that Green's functions in the dense coefficient matrix automatically satisfy the Sommerfeld radiation condition makes the BEM suitable for incorporation with the FEM as a coupled solver, where the vibro-acoustics of the structures are represented by the FEM, and external radiation is handled by the BEM (Wu and Chen, 2017; Jiang et al., 2018; Wu et al., 2019; Chen et al., 2024). However, the boundary integral is singular and requires additional treatments to obtain accurate solutions, thus complicating the numerical implementation, especially when a shallow-water environment is considered.

To overcome the problem of singular integrals and simplify numerical implementations, Koopmann et al. (1989) proposed the wave superposition method (WSM). The concept of replacing the radiation from the vibrating structure with the field generated by a group of equivalent sources offset from the structure surface circumvents the issue of integral singularity and reduces the computational cost by simplifying the numerical implementations. In addition, nonideal environments such as reverberation rooms and waveguides, can be easily handled by fitting Green's functions to the environment. Recently, coupled FEM/WSM solvers have been applied to sound field reconstruction of complex structures with low-frequency radiation fields in shallow waters (Wang and Guo, 2016; Zhang et al., 2020; Xi et al., 2023; Huang et al., 2019; He et al., 2023). In addition to the complex geometry of the structure that may affect the acoustic radiation in shallow water (Wang and Guo, 2016), the influence of seabed parameters (Zhang et al., 2020), water surface roughness Xi et al. (2023), and sound velocity profiles were preliminarily discussed by Huang et al. (2019). Acknowledging the applicability of the coupled FEM/WSM for arbitrary structures and complex underwater environments in the analysis of radiated noise from underwater vehicles over the last decade, we consider it a suitable candidate for our problem.

In the coupled FEM/WSM solver, the number of operations required to solve the exterior problem is typically $O(MNQ)$, where M is the number of equivalent source points, N is the computational complexity of the sound-propagation algorithm, and Q is the number of field points. Therefore, the computational cost of the coupled FEM/WSM solver significantly increases with distance, as long-range prediction requires a sufficient number of field points to achieve high resolution for identifying the detailed interference pattern of the waveguide. In addition, in the mid-to-high frequency range, the coupled FEM/WSM solver is cumbersome because the sound propagation algorithm becomes numerically expensive and M increases dramatically. The objective of this study is to propose an efficient and accurate approach for predicting long-range radiation from an arbitrary radiator in shallow water by deriving a semi-analytical solution. Although preliminary studies have discussed radiation from dipole and quadrupole sources in waveguides (Williams and Novak, 1974; Haug et al., 1975; Zhang and Zhu, 1987; Kuznetsov and Stepanov, 2017), further research is required to accommodate both the arbitrary radiation directionalities and the stratified inhomogeneous medium into a compact, semi-analytical solution representing structural radiation in shallow water.

In this paper, we propose a hybrid scheme for predicting the radiation from an arbitrary structure in a stratified shallow-water waveguide. The near-field prediction is given by combining the FEM vibro-acoustic analysis of the WSM exterior solver with Green's function calculated using the normal mode theory. In the far field, instead of numerically obtaining the source integral involved in the WSM, we derive a semi-analytical solution using the Fraunhofer approximation, providing a fast and accurate prediction of structural radiation in the ocean within seconds. The far-field condition under which our proposed semi-analytical solution is valid and discussed in detail. Such a condition is indeed useful for identifying the transition zone within which the radiated field of the vibrating structure in shallow water is dominated by the interference between each radiating patch of the source. Once the propagation range exceeds this zone, the radiated field is characterized by the source directionality and propagation mode. Therefore, the identification of the transition zone has potential applications in passive sonar detection. The remainder of this paper is organized as follows. Section 2 describes the coupling theory between structural vibration and acoustic radiation. Section 3 presents the derivation of the semi-analytical solution for calculating the far-field radiation from a structure in shallow water, including the calculation of radiation directionality using the coupled FEM/WSM solver, and the derivation of the normal-mode expression for the waveguide field produced by arbitrary directional sources. In Section 4, the proposed method is validated by comparing it with the benchmark finite element (FE) solution for both the Pekeris waveguide and a waveguide with a sound speed profile. The critical distance between the near and far fields of structural radiation in shallow water is discussed. Finally, Section 5 provides conclusions and an outlook for future work.

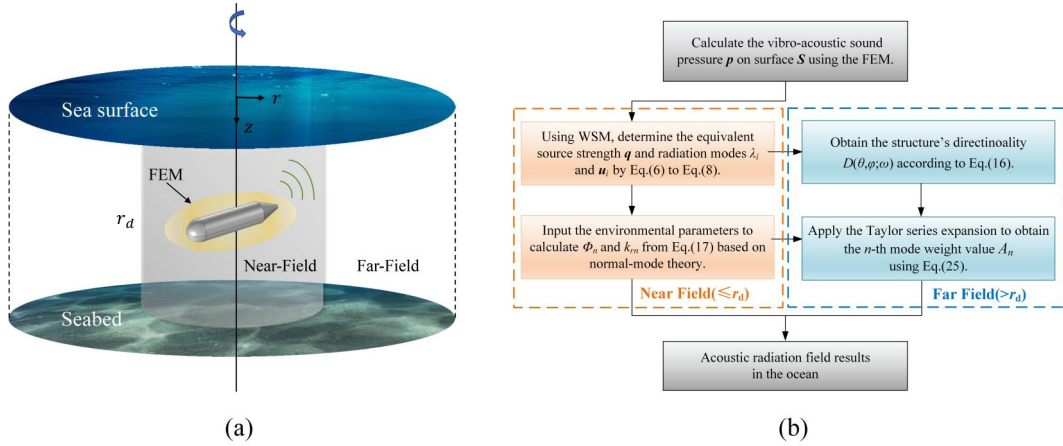


Figure 1: (a) Schematic diagram for calculating the radiated acoustic field. (b) Flowchart of the directional source method (DSM) for rapid prediction of acoustic radiation.

2. Theoretical FEM-WSM Model in the near-field region

Herein, a hybrid method is proposed to predict sound radiation from an elastic structure in a shallow-water waveguide. As depicted in Fig. 1, a range-independent waveguide with a stratified medium is considered in this paper. The acoustic-structure interaction is represented by the FEM with the acoustic-structural boundary established around the surface of the structure to couple the vibration and acoustics. The acoustic radiation outside the FEM domain, which is a Helmholtz exterior problem, is solved using the WSM. Unlike previous studies reported in the literature, the radiated field is divided into near- and far-field regions by a cylindrical surface with a radius of $r = r_d$. The cylindrical surface is axisymmetric to the z -axis, with the geometric center of the structure at this axis. The coupled FEM/WSM solver is implemented in the near-field region. Green's function in the WSM is calculated using the normal mode theory to automatically satisfy the boundary conditions at the sea surface and water-sediment interface. In the far-field region, where the detailed radiation pattern is distorted by the interference between multiple reflections, we derive an analytical solution for the integral of the equivalent sources with the waveguide Green's function, instead of numerically calculating it, as in the coupled FEM/WSM solver.

2.1. FEM for vibro-acoustic coupling analysis

To handle the acoustic-structure interaction, we implemented the FEM by enforcing continuities of pressure and particle velocity across the structure-fluid interface. Taking the harmonic time dependence $e^{j\omega t}$ and integrating the Helmholtz equation with the weights yields the FE discretization for the acoustic wave equation (Marburg and Nolte, 2008),

$$(\mathbf{K}_a + j\omega\mathbf{C}_a - \omega^2\mathbf{M}_a)\{\mathbf{p}_i\} = \{\mathbf{F}_a\} \quad (1)$$

where $j = \sqrt{-1}$ and ω is the angular frequency. Here, \mathbf{K}_a , \mathbf{C}_a , and \mathbf{M}_a denote the mass matrix, damping matrix, and stiffness matrix for acoustics, respectively; $\{\mathbf{p}_i\}$ represents the nodal pressures; and $\{\mathbf{F}_a\}$ represents the acoustic excitation.

For the elastic structure, the FE discretization for the motion vibration equation is given by

$$(\mathbf{K}_s + j\omega\mathbf{C}_s - \omega^2\mathbf{M}_s)\{\mathbf{u}_i\} = \{\mathbf{F}_s\} \quad (2)$$

where $\{\mathbf{u}_i\}$ are nodal displacements. In this case, \mathbf{M}_s , \mathbf{K}_s , and \mathbf{C}_s are the mass, stiffness, and damping matrices for the elastic structure system, respectively, and $\{\mathbf{F}_s\}$ represents the force loading on the nodes.

Across the interface, where the solid mechanics and pressure acoustics are coupled, the following boundary condition is enforced:

$$v_{an} = -\frac{1}{j\omega\rho_a} \frac{\partial p_i}{\partial n} = v_{sn} \quad (3)$$

where v_{sn} and v_{an} represent the normal velocity over the vibrating structure surface and the loading fluid, respectively.

Incorporating the boundary conditions given by Eq.(3) into Eq.(1) and Eq.(2), one can obtain a set of coupled equations

$$\left(\begin{bmatrix} \mathbf{K}_s & \mathbf{K}_c \\ 0 & \mathbf{K}_a \end{bmatrix} + j\omega \begin{bmatrix} \mathbf{C}_s & 0 \\ 0 & \mathbf{C}_a \end{bmatrix} - \omega^2 \begin{bmatrix} \mathbf{M}_s & 0 \\ -\rho_0 \mathbf{M}_c^T & \mathbf{M}_a \end{bmatrix} \right) \begin{bmatrix} \mathbf{u}_i \\ \mathbf{p}_i \end{bmatrix} = \begin{bmatrix} \mathbf{f}_s \\ \mathbf{f}_a \end{bmatrix} \quad (4)$$

where $\{\cdot\}^T$ denotes the matrix transpose and \mathbf{f}_s and \mathbf{f}_a represent the coupling force vectors on the structure and the underwater acoustic field.

In this study, all FEM matrices were assembled using the commercial software COMSOL Multiphysics, where the ocean waveguide is represented by the pressure acoustics module and the elastic structure is handled by the solid mechanics module. Solving the above coupled equation gives the wave field near the structure, which can then be used as an input to the WSM for either predicting the near-field radiation or generating the far-field directionality of each radiation mode of the structure.

2.2. Wave Superposition Method

The WSM is a numerical simplification of the Helmholtz integral. The key aspect is that the radiation from the vibrating structure can be replaced by field superposition owing to a set of equivalent sources within the structure. It is assumed that the number of equivalent sources is M .

The acoustic pressure at an arbitrary field point \mathbf{r} results from integrating the field produced by the equivalent sources, which can be discretized as follows:

$$p(\mathbf{r}) = \sum_m G(\mathbf{r}|\mathbf{r}_m) q_m(\mathbf{r}) \quad (5)$$

where q_m denotes the strength of the m -th source and $G(\mathbf{r}|\mathbf{r}_m)$ is the Green's function resulting from the source placed at \mathbf{r}_m . Lee (2017) suggests that the number of equivalent sources should be one-quarter to one-third of the collocation points to achieve convergent results.

Writing Eq.(5) in the matrix form yields

$$\mathbf{q} = \mathbf{G}^\dagger \mathbf{p} \quad (6)$$

where \mathbf{p} and \mathbf{q} are the vectors of sound pressure and source strengths, respectively. $\{\cdot\}^\dagger$ denotes the generalized matrix inverse. By providing the sound pressures calculated using the FEM within r_d , the strengths of the equivalent source can be obtained through Eq.(6). The Helmholtz exterior problem can then be solved by forward propagating the field generated by the equivalent sources using Eq.(5).

One of the purposes of this study is to reveal the coupling mechanism between structural acoustic radiation and underwater sound propagation, and to transform the solution for source strengths into acoustic radiation modes (Borgiotti, 1990). These modes are determined by the structure's geometry, frequency, and external fluid loading, and are independent of the material properties and the type of excitation.

Based on the WSM, one can obtain the radiation matrix \mathbf{R}

$$\mathbf{R} = \frac{k^2 \rho_0 c_0}{8\pi} \begin{bmatrix} 1 & \frac{\sin(kr_{12})}{kr_{12}} & \dots & \frac{\sin(kr_{1N'})}{kr_{1N'}} \\ \frac{\sin(kr_{21})}{kr_{21}} & 1 & \dots & \frac{\sin(kr_{2N'})}{kr_{2N'}} \\ \dots & \dots & \dots & \dots \\ \frac{\sin(kr_{N'1})}{kr_{N'1}} & \frac{\sin(kr_{N'2})}{kr_{N'2}} & \dots & 1 \end{bmatrix} \quad (7)$$

where r represents the distance between each pair of equivalent sources and N' denotes the total order of radiation modes. It is evident that \mathbf{R} is both real and symmetric, and given that the radiated sound power is always positive, \mathbf{R} must be positive definite.

Using eigenvalue decomposition, \mathbf{R} can be expressed as:

$$\mathbf{R} = \mathbf{U}^H \mathbf{S} \mathbf{U} \quad (8)$$

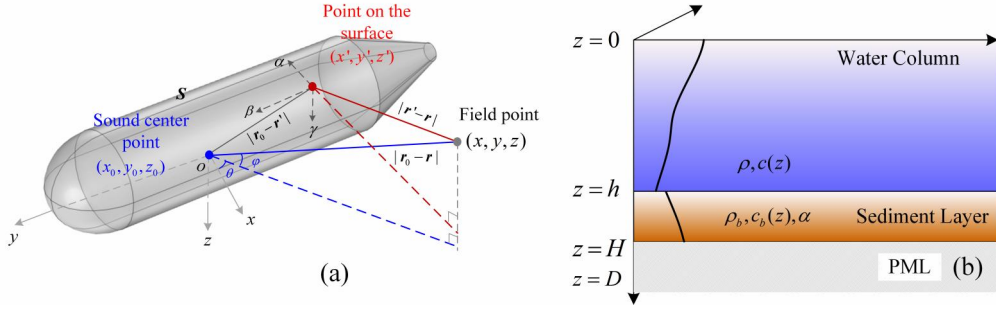


Figure 2: (a) The far-field approximation diagram of the structural model. (b) Schematic of a bare hull model under point force excitation, completely submerged in a shallow-water waveguide. $\rho, c(z)$ represent the water density and sound speed, respectively, while $\rho_b, c_b(z)$ and α denote seabed density, speed, and attenuation, respectively. The parameters h, H, D correspond to the water depth, seabed depth, and perfectly matched layer (PML) cut-off depth, respectively.

where \mathbf{S} is a real diagonal matrix with diagonal elements s_i representing the eigenvalues in descending order and $\{\cdot\}^H$ denotes the conjugate transposition. The column vector \mathbf{u}_i of \mathbf{U} corresponds to the eigenvector associated with the i -th acoustic radiation mode. Because s_i are sorted in descending order, the higher the order of the radiation modes, the lower their radiation efficiencies.

By representing the source strength in terms of acoustic radiation modes, one can obtain

$$\mathbf{q} = \sum_i \lambda_i \mathbf{u}_i \quad (9)$$

where λ_i is the expansion coefficient of the i th radiation mode. Once the λ_i of the sound radiation mode is obtained, the sound pressure and particle velocity at any point in the sound field can be reconstructed.

3. Fast prediction of long-range radiation

Although the WSM offers a solution that covers both near-field and far-field radiation, its efficiency depends on the number of equivalent sources and the field points to be predicted, and suffers from a dramatic decline when considering long-range prediction at mid to high frequencies, especially in shallow water. To solve this problem, the following analysis is performed to derive an analytical solution for the waveguide field produced by a structural source in the far-field region. This begins with a general derivation of the free-field situation, which is then extended to the waveguide scenario.

3.1. Free field

Acoustic radiation from a vibrating structure can be considered as the summation of the fields due to different order acoustic radiation modes.

$$p(\mathbf{r}') = \int_S \mathbf{q}(\mathbf{r}') G(\mathbf{r}; \mathbf{r}') d\mathbf{r}' = \sum_i \lambda_i \int_S \mathbf{u}_i(\mathbf{r}') G(\mathbf{r}; \mathbf{r}') d\mathbf{r}' \quad (10)$$

where $G(\mathbf{r}; \mathbf{r}')$ is the free-field Green's function expressed as follows:

$$G(\mathbf{r}; \mathbf{r}') = \frac{e^{-jk|\mathbf{r}' - \mathbf{r}|}}{|\mathbf{r}' - \mathbf{r}|} \quad (11)$$

where $\mathbf{r}' = (x', y', z')$ and $\mathbf{r} = (x, y, z)$ represent the positions of the source and field points, respectively.

Next, when $R_0 > k|\mathbf{r}' - \mathbf{r}_0|^2/2\pi$, $R_0 = |\mathbf{r}_0 - \mathbf{r}|$ indicates the distance between the acoustic center of the structure and the field point, and we introduce the Fraunhofer approximation to $k|\mathbf{r}' - \mathbf{r}|$ in the far field (Goodman, 2005) :

$$k|\mathbf{r}' - \mathbf{r}| \cong k|\mathbf{r}_0 - \mathbf{r}| + k \frac{|\mathbf{r}' - \mathbf{r}_0|^2}{2|\mathbf{r} - \mathbf{r}_0|} - k(\alpha \cos \theta \sin \phi + \beta \cos \theta \cos \phi + \gamma \sin \phi) \quad (12)$$

where (θ, ϕ) is the far-field observation angle; θ and ϕ represent the azimuth and elevation angles, respectively; and $\mathbf{r}_0 = (x_0, y_0, z_0)$ represents the acoustic center of the structure. See Fig. 2(a) for details.

In general, the second-order term in the phase factor can be ignored because $kL_a^2/(2|\mathbf{r} - \mathbf{r}_0|) < \pi$ where L_a is the maximum size of the structure. This yields

$$k|\mathbf{r}' - \mathbf{r}| \approx k|\mathbf{r}_0 - \mathbf{r}| - k(\alpha \cos \theta \sin \phi + \beta \cos \theta \cos \phi + \gamma \sin \phi) \quad (13)$$

where the local coordinates of the equivalent source are given by

$$\begin{cases} \alpha = x' - x_0, \\ \beta = y' - y_0, \\ \gamma = z' - z_0, \end{cases} \quad (14)$$

The far-field expression for the structural acoustic radiation in the free space can then be obtained by substituting the Eq.(11) to Eq.(14) back into Eq.(10), the integral form in Eq.(10) can be simplified into the product of point source Green's function and the directionality of the radiation source (Zhang, 1964),

$$p_f(x, y, z; \omega) = \frac{e^{-jk|\mathbf{r}_0 - \mathbf{r}|}}{|\mathbf{r}_0 - \mathbf{r}|} D(\theta, \phi; \omega) = \frac{e^{-jk|\mathbf{r}_0 - \mathbf{r}|}}{|\mathbf{r}_0 - \mathbf{r}|} \sum \lambda_i D_i(\theta, \phi; \omega) \quad (15)$$

where $D(\theta, \phi; \omega)$ denotes the directionality of the structure and $D_i(\theta, \phi; \omega)$ denotes the directionality of the i -th radiation mode of the structure, expressed as

$$D_i(\theta, \phi; \omega) = \int_S \mathbf{u}_i(x_0 + \alpha, y_0 + \beta, z_0 + \gamma) \times e^{-jk(\alpha \cos \theta \sin \phi + \beta \cos \theta \cos \phi + \gamma \sin \phi)} d\alpha d\beta d\gamma \quad (16)$$

The derivation above indicates that the range and angle are variably separable in the form of far-field radiation. The directional factor $D_i(\theta, \phi; \omega)$ determines the spatial distribution of radiation. The term monopole essentially indicates that far-field radiation exhibits spherical spreading. Nevertheless, in the near-field region where $|\mathbf{r} - \mathbf{r}_0|$ is comparable to L_a , the second-order term in Eq.(12) cannot be ignored, so the contribution of $|\mathbf{r}' - \mathbf{r}_0|$ must be considered in the integration in Eq.(16). Therefore, in the near field, the range and angle are coupled, indicating that the radiation does not follow any simple laws and may exhibit interference patterns.

3.2. Waveguide field

We now consider the radiated field generated by the same structure in a shallow-water waveguide. As shown in Fig.2(b), the water sound speed c and seabed sound speed c_b vary with depth. Analogous to Eq.(10), a similar expression for the radiated field can be obtained by replacing the free-field Green's function with the waveguide Green's function. In this study, we employ the normal mode theory to describe the waveguide Green's function.

Based on the normal-mode model, the waveguide Green's function is given by (Jensen et al., 1995),

$$G(r, z) = C \sum_0^\infty \Phi_n(z) \Phi_n(z') \frac{e^{jk_{rn}r}}{\sqrt{k_{rn}r}} \quad (17)$$

where the coefficient $C = je^{-j\pi/4}/(4\rho(z')\sqrt{8\pi})$, $H_0^{(1)}(\cdot)$ represents the first kind Hankel function of zero-order, $\Phi_n(z)$ is the mode shape function, and k_{rn} is the horizontal wavenumber. The Sturm–Liouville eigenproblem associated with k_{rn} needs to be solved. When the depth-dependent sound speed is considered, numerical approaches are required to solve the eigenproblem. Unlike root finder algorithms, which have been widely applied in solving eigenproblems (Porter, 1992), the multimodal method (Bi et al., 2007; Liu and Li, 2021; He et al., 2021, 2024), also called the modal projection

method, is used here because it accurately addresses the contribution of branch cuts to near-field propagation, which most existing normal-mode methods cannot. This is a key aspect of our approach, because near-field radiation needs to be considered when analyzing the critical range within which the far-field formulation derived here is invalid.

Substituting Eq. (17) back into Eq. (10), the solution for structural acoustic radiation in shallow water can be obtained as follows:

$$p_w(x, y, z) = C \sum_{n=0}^{\infty} \Phi_n(z) \sum_i \lambda_i \int_S \mathbf{u}_i(x', y', z') \Phi_n(z') \frac{e^{jk_{rn}R'}}{\sqrt{k_{rn}R'}} dx' dy' dz' \quad (18)$$

where $R' = \sqrt{(x - x')^2 - (y - y')^2}$ represents the horizontal distance between the equivalent source and field point. Note that, unlike in free space, the frequency in the waveguide of radiation acoustic propagation should be higher than the waveguide cutoff frequency f_c to ensure that sound propagates over long distances. Typically, for a Pekeris waveguide, the cutoff frequency is given by $f_c = cc_b/(4h\sqrt{c_b^2 - c^2})$, where c and c_b are the sound speeds in water and sediment, respectively, and h is the water depth (Jensen et al., 1995). Otherwise, sound waves can propagate only through the sediment and rapidly attenuate, making long-range propagation predictions meaningless.

Direct discretization of the above equation yields the formulation of the WSM solution for structural acoustic radiation in shallow water:

$$p_w(x, y, z) = C \sum_i \lambda_i \sum_{n=0}^{\infty} \Phi_n(z) \sum_m \mathbf{u}_i(x'_m, y'_m, z'_m) \Phi_n(z'_m) \frac{e^{jk_{rn}R'_m}}{\sqrt{k_{rn}R'_m}} dx' dy' dz' \quad (19)$$

where the subscript m indicates the m -th equivalent source. The above formulation was used in this study to couple the FEM for predicting the near-field radiation in shallow water.

Here, we assume that $k_{rn}L_a^2/R_0 < 1$, introducing the Fraunhofer approximation in the horizontal plane and ignoring the second-order term yields

$$\begin{aligned} k_{rn}|\mathbf{r}' - \mathbf{r}| &\cong k_{rn}|\mathbf{r}_0 - \mathbf{r}| - k_{rn}(\alpha \cos \theta + \beta \sin \theta) \\ &= k_{rn}|\mathbf{r}_0 - \mathbf{r}| - k(\alpha \cos \theta \cos \phi_n + \beta \sin \theta \cos \phi_n) \end{aligned} \quad (20)$$

where $\phi_n = \tan^{-1}(k_{zn}/k_{rn})$ denotes the grazing angle of the plane wave of the n -th order.

Using this approximation to simplify the integral A_n , we obtain

$$p_w(r, z) = C \sum_i \lambda_i \sum_{n=0}^{\infty} \frac{A_n}{\sqrt{k_{rn}}} \Phi_n(z) \frac{e^{-jk_{rn}R_0}}{\sqrt{R_0}} \quad (21)$$

$$A_n = \int_S \mathbf{u}_i(x_0 + \alpha, y_0 + \beta, z_0 + \gamma) \Phi_n(z') e^{jk(\alpha \cos \theta \cos \phi_n + \beta \sin \theta \cos \phi_n)} d\alpha d\beta d\gamma \quad (22)$$

Next, we assume that the depth derivative of the sound velocity at depth, where the source is imposed, is negligible. Specifically, when $|d(z)L_z^3| \ll 1$ is satisfied (where L_z is the dimension of the structure in the vertical direction, and $d(z) = d(k(z)^2)/dz$ represents the quadratic derivative of the vertical wavenumber), the depth derivative of the mode function is approximately zero.

Under this assumption, we perform a Taylor series expansion of $\Phi_n(z')$ at depth z_0 and reduce the order of the expanded series terms by sorting them into even and odd orders:

$$\begin{aligned} W_n &= W_{n,odd} + W_{n,even} \\ &= \sum_{b=0} \frac{1}{(2b+1)!} \left. \frac{d^{2b+1}\Phi_n(z)}{dz^{2b+1}} \right|_{z=z_0} \gamma^{2b+1} + \sum_{b=0} \frac{1}{(2b)!} \left. \frac{d^{2b}\Phi_n(z)}{dz^{2b}} \right|_{z=z_0} \gamma^{2b}, \\ &= \left. \frac{d\Phi_n(z)}{dz} \right|_{z=z_0} \frac{\sin(k_{zn}\gamma)}{k_{zn}} + \Phi_n(z_0) \cos(k_{zn}\gamma). \end{aligned} \quad (23)$$

where k_{zn} denotes the n -th vertical wavenumber. The reduced order of the expanded series is obtained using the eigenequation $[d^2/dz^2 + (k^2 - k_{rn}^2)]\Phi_n = 0$. By substituting the above equation into Eq. (22), we obtain:

$$A_n = \int_S \mathbf{u}_i(x_0 + \alpha, y_0 + \beta, z_0 + \gamma) \left[\frac{d\Phi_n(z)}{dz} \Big|_{z=z_0} \frac{\sin(k_{zn}\gamma)}{k_{zn}} + \Phi_n(z_0) \cos(k_{zn}\gamma) \right] \frac{e^{jk(\alpha \cos \theta \cos \phi_n + \beta \sin \theta \cos \phi_n)}}{\sqrt{k_{rn}R}} d\alpha d\beta d\gamma, \quad (24)$$

By applying the Euler equation to convert the sine and cosine terms in the above equation into exponential functions and then using the relation $k_{zn} = k \sin \phi_n$, the integral appearing in A_n can be replaced with a function of directionalities $D_i(\theta, \phi)$ as described in Eq.(16). This yields

$$\begin{aligned} A_n &= A_{n,odd} + A_{n,even} \\ &= \frac{-j}{2} \frac{d\Phi_n(z)}{dz} \Big|_{z=z_0} \frac{1}{k_{zn}} [D_i(\theta, \phi_n) - D_i(\theta, -\phi_n)] + \frac{1}{2} \Phi_n(z_0) [D_i(\theta, \phi_n) + D_i(\theta, -\phi_n)] \end{aligned} \quad (25)$$

The analytical solution for the structural acoustic radiation in shallow water is given by Eq.(21). The derived solution suggests that after obtaining the directionality of each radiation order using the coupled FEM/WSM solver, as described in Section 2 and Section 3.1, the far-field acoustic radiation in shallow water can be rapidly predicted by simply running a normal-mode code only once.

It is noteworthy that Eq. (21) directly reveals the coupling between acoustic radiation modes and propagation modes, suggesting that each radiation mode acts as a modal filter potentially exciting specific normal modes by the weighting function $D_i(\theta, \phi)$, which varies with the order of the radiation mode. In addition, this analytical solution can be applied to horizontally stratified ocean environments with arbitrary sound speed profiles (SSPs). We refer to this as the directional source method (DSM), which is used to approximate the far-field radiation field. The algorithm flowchart we proposed is shown in Fig. 1(b).

Next, we consider the special case in which the acoustic radiation mode is symmetric with respect to the $z = 0$ plane, which implies that $D_i(\theta, -\phi) = D_i(\theta, \phi)$. Then

$$A_{o,odd} = 0, \quad A_{n,even} = \Phi_n(z_0) D_i(\theta, \phi_n). \quad (26)$$

Eq.(22) then becomes

$$p_w(r, z) = C \sum_i \lambda_i \sum_{n=0}^N D_i(\theta, \phi_n) \Phi_n(z_0) \Phi_n(z) \frac{e^{-jk_{rn}R_0}}{\sqrt{k_{rn}R_0}} \quad (27)$$

The radiated sound pressure level (SPL) is defined as

$$\text{SPL} = 20 \log_{10} \frac{p}{p_0} \quad (28)$$

where p_0 is the reference sound pressure for an underwater acoustic environment (equal to 1 μPa).

3.3. The critical range distinguishing the near to far field of structural radiation in shallow water

In the Fraunhofer approximation, by ignoring near-field effects, the far-field radiation is reduced to the point-source field multiplied by the directionality function. In other words, the characteristics of the near-field radiation are absent in the analytical solution derived above. Therefore, it is essential to determine the critical range beyond which the proposed analytical solution is invalid.

Indeed, we can obtain the critical distance expressed by r_d , based on the far field condition $r > r_d$, for which the Fraunhofer approximation is valid. This implies that $k_0 L_a^2 / (2|\mathbf{r} - \mathbf{r}_0|) < \pi$, which indicates that the second-order term in Eq.(12) can be ignored. Generally, the effective area that emits radiation is smaller than the overall surface of the radiator. The condition $r > L_a$ indicates that the critical distance should be greater than at least one length of the structure. Therefore, the far-field condition can be further extended to

$$r > L_a^2 k_0 / 2\pi, \quad r > L_a \quad (29)$$

When considering the shallow water scenario, the far-field condition becomes horizontal wavenumber dependent, and the frequency of the acoustic field should be greater than the cutoff frequency f_c of the waveguide to ensure far-field propagation of the radiated sound source, which gives

$$r > L_a^2 k_{rn} / 2\pi, \quad r > L_a \quad (30)$$

Note that r_d now depends on the number of normal modes since different normal modes travel at different modal phase speeds in the waveguide. Eq.(30) can be rewritten as $r > L_a^2 f / c_{pn}$, where c_{pn} represents the phase speed of the n th normal mode. Since c_{pn} is always less than c_0 , the condition $k_{rn} L_a^2 / (2|\mathbf{r} - \mathbf{r}_0|) < \pi$ is satisfied if Eq.(29) holds.

Furthermore, as the k_{rn} can be further simplify in ideal waveguide, Eq.(30) changes to ,

$$r > L_a^2 \sqrt{k_0^2 - \pi^2 / h^2} / 2\pi, \quad r > L_a \quad (31)$$

This equation highlights the relationship between the critical distance, sea depth, and frequency. The detailed discussion on the influence of the environment parameter and mode number on the critical range is presented in Section 4.4.

4. Numerical Results

The vibrating shell model with point-force excitation was first performed using the FEM to verify the accuracy of the proposed method for predicting structural acoustic radiation in a Pekeris waveguide. Next, near-field calculations using the conventional coupled FEM/WSM scheme and far-field results provided by the proposed analytical solution were compared in detail, with the critical distance distinguishing them discussed for various parameters, including frequency, radiator size, and water depth. Additionally, the coupling mechanism between the structural acoustic radiation and underwater sound propagation was revealed by presenting a frequency-range spectrum analysis using the proposed method.

4.1. Verification of Sound Field Radiated based on spherical shell in Pekeris waveguide

The proposed method was validated by comparison with a two-dimensional (2D) axisymmetric finite element method (FEM) of a vibrating spherical shell in a Pekeris waveguide. This serves as a benchmark FE model for testing. A simple and common scenario assuming an isovelocity water column under a flat sea surface is considered (Kha et al., 2023; Huang et al., 2019; Qian et al., 2022). A corresponding 2-D finite element model, shown in Fig.3, is created using the commercial software COMSOL Multiphysics (v6.1) and used to generate appropriate results for model verification of the analytical procedure.

The elastic shell and surrounding fluid domain were modeled using pressure acoustics and solid mechanics modules in 2D axisymmetry, respectively. Perfectly matched layers (PMLs) were used to truncate the finite fluid domain and absorb reflections from the outer boundaries. The thickness of the PML layer is three times of the wavelength. The fluid domain is discretized using tetrahedrons with a minimum mesh size of $\lambda/7$. The mesh density in the blue area near the shell is increased threefold. At the surface of the shell, water-seabed interface, and fluid-solid interface, where significant and complex coupling may occur, the meshing density was increased tenfold (Isakson and Chotiros, 2011). The FEM meshing model for water, structure, seabed, and PML implemented in the COMSOL software is shown in Fig.3.

The water depth h of the Pekeris waveguide is 100m. The seabed depth H is 200m. The density and sound speed of the water are $\rho = 1000 \text{ kg/m}^3$ and $c = 1500 \text{ m/s}$, respectively. The seafloor has a density of $\rho_b = 2000 \text{ kg/m}^3$ and a sound speed of $c_b = 1800 \text{ m/s}$ with an attenuation α of $0.4 \text{ dB}/\lambda$. The spherical shell was placed at a source depth of 50 m, excited by a vertical downward point force $F_s = 100\text{N}$ at the top of the shell (the location is $(x = 0, y = 0, z = 40\text{m})$). The radius is 10 m, and the thickness is 20 mm, the material used is steel (type = AISI 4340). The density, Young's modulus, and Poisson's ratio of the shell are $\rho_s = 7850 \text{ kg/m}^3$, $E_s = 2 \times 10^{11} \text{ Pa}$, and $\nu_s = 0.33$, respectively. The simulation parameters for the environment and the shell model are summarized in the Fig.3.

The proposed method is verified by comparing the results with those from an FEM simulation using COMSOL. Fig.4 extracts the radiated field predicted by different approaches along $z = 50 \text{ m}$ when the excitation frequency is 50Hz and 100Hz, respectively. The proposed analytical solution approaches the results obtained by the other two methods, within 0.1 dB difference observed at long ranges. However, the near-field prediction by the analytical solution exhibited an obvious disparity compared to the other two, which was caused by the far-field approximation used to derive the analytical solution. A detailed discussion of this near- to far-field transition behavior is presented in the next section.

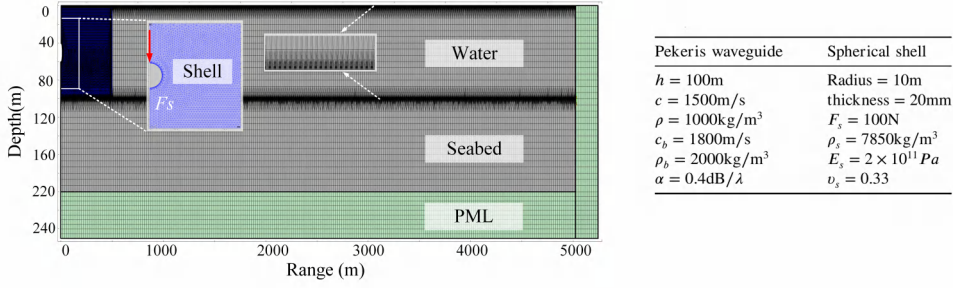


Figure 3: The schematic diagram shows an elastic spherical shell in shallow water with a 2D FEM mesh under the axisymmetric condition using the commercial software COMSOL, along with the corresponding simulation parameters.

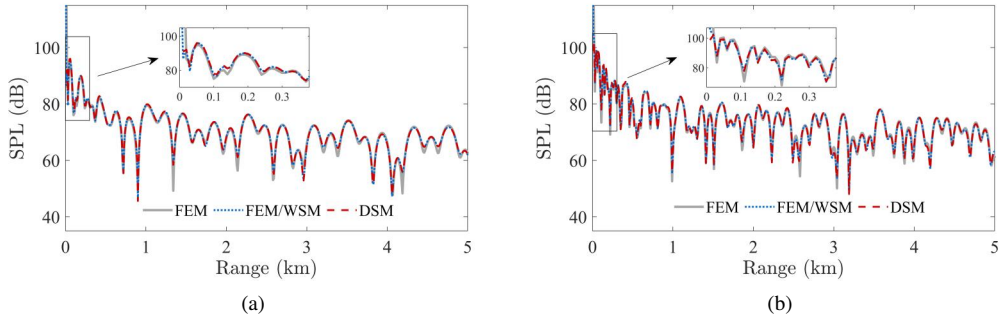


Figure 4: The SPLs in a benchmark model are calculated using the different methods at depth $z = 50\text{m}$ in (a) and (b), corresponding to 50Hz and 100Hz, respectively. The gray solid line, the blue dotted line, and red dashed line represent the FEM, FEM/WSM, and DSM, respectively.

4.2. Discussion of the characteristics of the radiated field produced by a simplified model for an underwater vehicle in shallow water

4.2.1. Near-field and far-field radiation

First, we analyze the acoustic radiation from the vibrating shell of an underwater vehicle in short ranges using the FEM/WSM. The shell is a simplified submarine model with a hemispherical front end, a cylindrical middle section, and a conical rear end. As shown in Fig.5(a), the total length of model is 70 m, the height of the conical platform is 10 m, and the upper radius of the conical platform is 2m. In this case, we simulated a deeper ocean at a water depth of $h=200\text{ m}$. The other parameters of the underwater environment were identical to those used in the previous benchmark case. The shell was placed at $z_s=100\text{ m}$. A harmonic point force was applied at the upper central position of the shell with an amplitude of 100 N and an excitation frequency of 100 Hz. A schematic of the geometric configuration and the meshing scheme implemented in the FE model is shown in Fig.5(a)~(b).

Fig.6 presents a comparison of the near-field radiation in the free field and the shallow water in the $y = 0\text{ m}$ and $z = 100\text{ m}$ planes, respectively. It is evident that the radiated field generated by the vibrating shell exhibits an observable spatial distribution characterized by the radiation mode excited by the point-force on the central hull. Therefore, the horizontal radiation is symmetric with respect to the $y=0\text{ m}$ plane. Because the excitation force is vertical, most of the energy is radiated toward the directions with large grazing angles relative to the horizontal in the free field. This creates shadow zones ahead of and behind the shell in the $y=0\text{ m}$ plane, over which the radiated noise can barely be heard. In fact, the constructive and destructive patterns in free-field radiation result from the interference between the emissions from each radiating patch of the shell. However, in shallow water, boundary reflection causes energy traveling with large grazing angles, which is rapidly attenuated in short ranges. Conversely, the energy deflected by small grazing angles relative to the horizontal can propagate within the waveguide to long ranges, creating a denser interference pattern that compensates for the shadow zones observed in the free-field case. This dense interference pattern was caused by the coherent interactions between the different propagation modes of the waveguide rather than

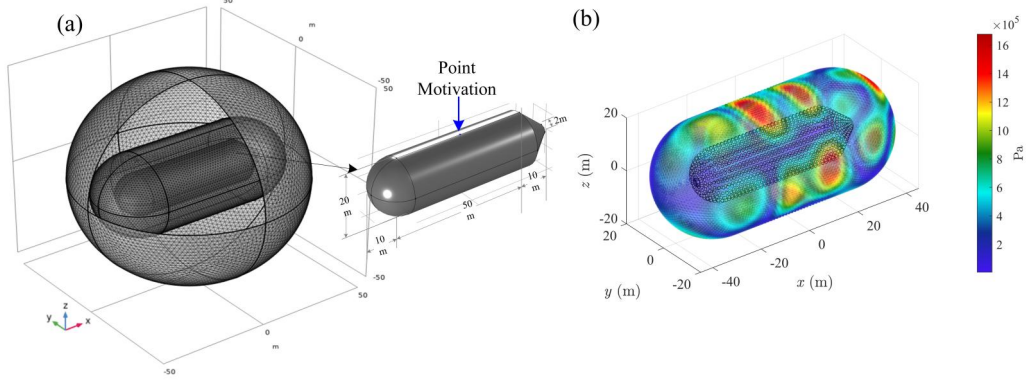


Figure 5: (a) Details of the naked hull model and the mesh in COMSOL. (b) 3D pressure distribution of the capsule's wrapping surface in free space and the locations of the equivalent sources.

the radiation modes of the vibrating hull. This indicates that the coupling mechanism between the structural acoustic radiation and underwater sound propagation is complicated, potentially involving energy transfer from the radiation mode to the propagation mode according to the grazing angle of the acoustic wave. This is discussed in detail in Section 4.2.3.

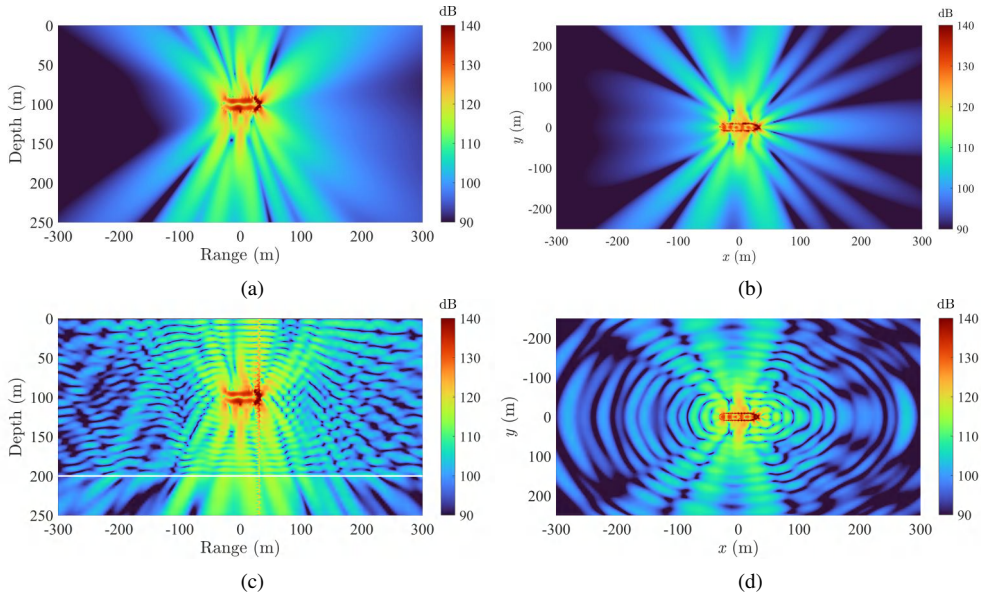


Figure 6: Near-field SPLs in the $r - z$ and $x - y$ spaces. (a) and (b) show results in free space, while (c) and (d) present results in the Pekeris waveguide. The white line in (c) indicates the location of the seabed. The acoustic field frequency is 100Hz.

Next, we compared the long-range calculations predicted by the FEM/WSM and the proposed analytical solution at different frequencies, as shown in Fig. 7. There is good consistency between the two solutions are observed, indicating that the proposed analytical solution can accurately describe the intricate coupling between the radiation modes and propagation modes. A detailed observation of these results suggests that the long-range structural acoustic radiation in shallow water only exhibits an interference pattern due to phasing in range, which causes the propagating modes to sum constructively or destructively. The characteristics of the radiation from the hull vanish rapidly as the range increases, which coincides with the leaky energy observed in Fig. 6. This confirms that only the energy traveling at small grazing

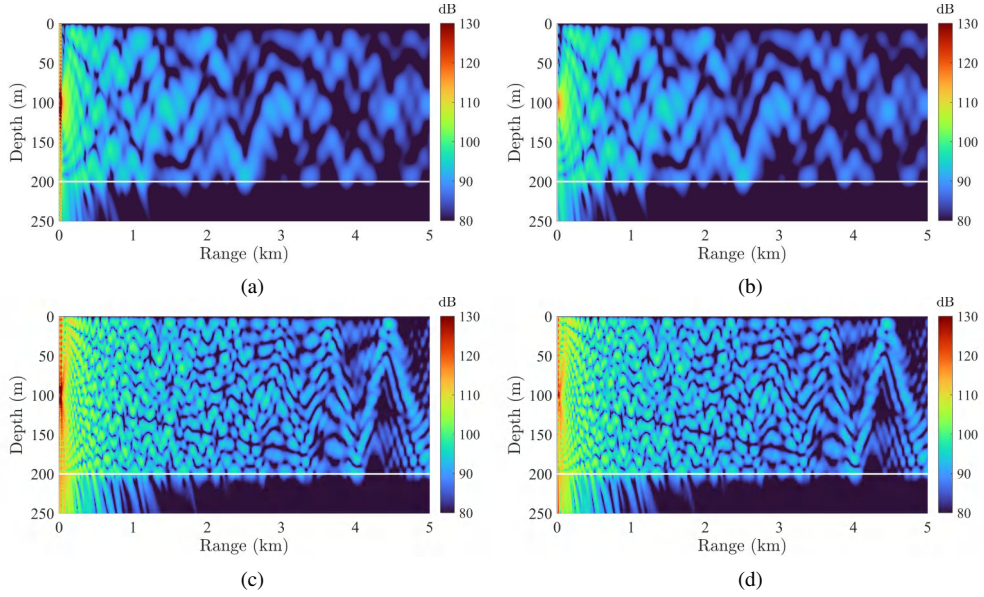


Figure 7: Far field SPLs in the Pekeris waveguide, shown in the $r - z$ space. The upper row presents results at 50 Hz, and the lower row at 100 Hz. (a) and (c) display results from FEM/WSM, while (b) and (d) show results from DSM.

angles can couple with the propagating modes. This indicates that the structural acoustic radiation in shallow water acts as a directional point source and selectively excites certain propagating modes with specific weights. These weights can be accurately described by Eq.(21), which is determined by the far-field directionality of the radiation mode.

We then analyzed the relative error distribution between the two solutions in the horizontal plane. The relative error is defined as $\Delta \text{SPL} = \text{SPL}_{\text{WSM}} - \text{SPL}_{\text{DSM}}$, where SPL_{WSM} and SPL_{DSM} represent the SPLs calculated using the coupled FEM/WSM solver and the proposed analytical solution, respectively.

Fig.8 shows the relative error at 50Hz and 100Hz, respectively. In the free-field case, the errors are significant in the region where the trough of the radiated field (coinciding with the minimum of the source directionality shown in Fig.8(a)) occurs. This can be interpreted by the fact that this trough, when discussed in relation to the shadow zone observed in Fig.6, is caused by the interference between different radiating patches, a mechanism that is absent when representing the field solely by a directional point source. Therefore, one can indeed observe that the errors in the shallow-water case exhibit a similar increase associated with the troughs of the radiated field, which does not reflect any underlying issue associated with the derived analytical solution. Moreover, owing to the presence of boundary reflections, additional troughs were created by the interference between different propagating modes, resulting in an increase in the regions where the errors were significant.

4.2.2. Shallow water with sound speed profiles

Based on the derivation of the proposed analytical solution, we assume that the depth derivative of the vertical wavenumber at the source depth is negligible to achieve an order reduction for the Taylor series of eigenfunctions. This means that the SSP in shallow water should vary smoothly with depth. However, we assert that this assumption is reasonable under most circumstances because realistic SSPs can easily satisfy the condition for which the assumption is valid. The proposed analytical solution was verified using a shallow waveguide with SSPs. As shown in Fig.9, two typical SSPs were considered, that is, the negative SSP, $c(z) = c_1 - gz$, and the tanh SSP, $c(z) = c_2 - d \tanh(z - z_0/\sigma)$, where $c_1 = 1525 \text{ m/s}$, $g = 0.25 \text{ s}^{-1}$, $c_2 = 1800 \text{ m/s}$, $d = 30 \text{ s}^{-1}$, $z_0 = 100 \text{ m}$, and $\sigma = 10$.

Excellent agreement with the solution predicted by the coupled FEM/WSM solver is shown in Fig.9(c), where the SPL is plotted as a function of range at a receiver depth of 100 m. This demonstrates that the proposed analytical solution is accurate, even when the sound speed gradient at the source depth is significant. This proves that the proposed analytical solution works well for shallow water with smoothly varying SSPs, which closely represents the most realistic situations. In addition, in the presence of different SSPs, the interference patterns in the SPLs shift and change, which is

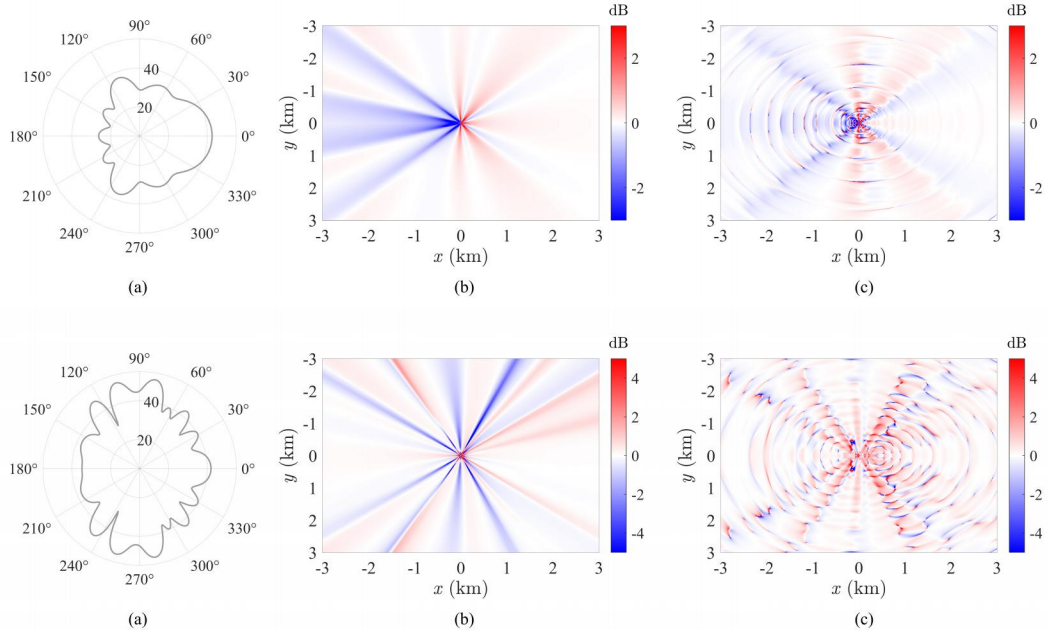


Figure 8: Calculation errors of the radiated acoustic field in $x - y$ space with azimuth distribution between FEM/WSM and DSM. The upper row shows results at 50 Hz, and the lower row at 100 Hz. (a) and (d) present the directionalities $D(\theta, 0^\circ)$, (b) and (e) show the error distributions in free space, and (c) and (f) show the error distribution in the Pekeris waveguide.

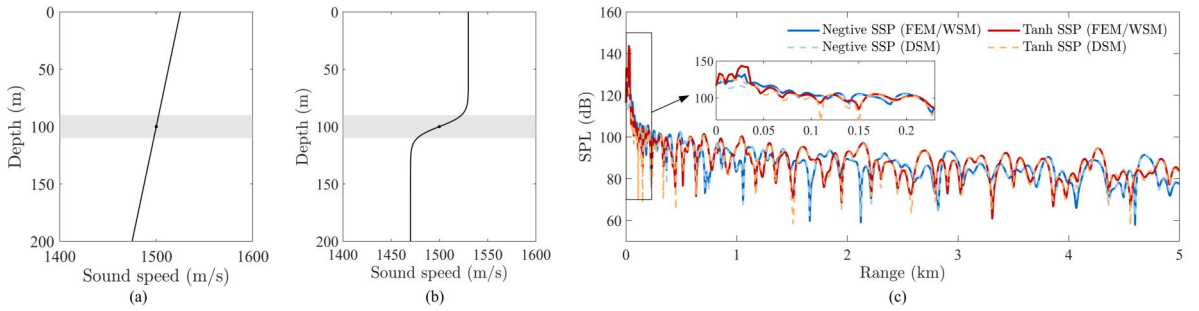


Figure 9: (a) and (b) show the SSPs for the negative and tanh waveguides, respectively. The gray rectangular area indicates the depth range occupied by the submerged structure. (c) shows the SPLs at frequency $f = 100$ Hz and depth $z_s = 100$ m. The blue solid line and dashed line represent the SPLs of the FEM/WSM and DSM in the negative SSP, respectively, whereas the red solid line and dashed line represent the corresponding results in the tanh SSP.

caused by the effect of refraction, alerting the arrival path and delay. The above results confirm that the distribution of structural acoustic radiation in shallow water is sensitive to SSPs, and that the proposed analytical solution can handle situations in which the sound speed of water varies with depth.

4.2.3. Coupling mechanism between the radiation modes and the propagation modes

In this section, we analyze the coupling mechanism between the radiation modes and the propagation modes by simulating the broadband acoustic field produced by the same shell structure used in the previous simulation.

The parameters simulated in this case are the same as in Section 4.2.2. The receiver is deployed at an azimuth angle of $\theta = 0^\circ$ with respect to the y axis, along which the axis of the shell is placed, and the receiver depth is $z = 100$ m. The frequency-range interference structure of the radiated sound field in the LOFAR spectrum was simulated by

repeatedly running the proposed model over different frequencies, with the near-field and far-field results computed by the coupled FEM/WSM solver and the analytical solution, respectively. Note that only mechanical radiation noise is considered here. The corresponding results are shown in Fig.10, where the white dashed line marked by L_a^2/λ distinguishes the critical distance between the near-field and far-field radiation. The transition behavior between the near-field and far-field radiation varies smoothly, although the results are given by two solvers depending on the ranges. This confirms the effectiveness of the proposed model.

Fig.10 exhibits two types of interference patterns in the frequency-range domain. We hypothesize that the oblique fringes result from constructive and destructive interference between the propagation modes of the ocean waveguide, the slopes of which are determined by the waveguide invariants β (Chuprov and Brekhovskikh, 1982). β is invariant with respect to the frequency-to-range ratio, which is supposed to exhibit a constant slope in the frequency-range domain. Here, we annotate $\beta_{(1,2)}$, $\beta_{(1,3)}$, and $\beta_{(2,3)}$ on the frequency-range spectrum, where the subscripts indicate the numbers of the modes causing the interference. The fact that the annotated β coincides with the slope interference pattern validates our hypothesis.

The stronger horizontal interference fringes are, on the other hand, determined by the characteristics of the structural acoustic radiation, that is, $D(\theta, \phi; \omega)$. The directional function $D(\theta, \phi; \omega)$ at $\theta = 0^\circ$ is shown in the right panel of Fig.10 as a function of frequency. The grazing angle $\phi = 0^\circ$ was chosen because low-order modes that tend to contribute to long-range propagation interact with the radiated energies traveling at small grazing angles, based on the analytical expression given in Eq.(21). Evident peaks in $D(\theta, \phi; \omega)$ coincide with the significant horizontal fringes presented in the frequency-range spectrum, suggesting that they are featured by the radiator rather than the waveguide.

The far-field normalized directionality of the first eight acoustic radiation modes $|D_i^{\text{norm}}(\theta, \phi)|$ ($i = 1, \dots, 8$) at 81Hz, where one of the obvious peaks is observed in the frequency spectrum of $D(\theta, \phi)$, is shown in Fig.11. Here, the normalized directionality is defined as $D_i^{\text{norm}}(\theta, \phi) = D_i(\theta, \phi)/D^{\text{max}}(\theta, \phi)$, where the denominator is the maximum value among all modes. It can be observed that the first and fourth modes are circumferential modes, whose radiated energy is concentrated along the cylindrical axis. This means that most of their energy radiates towards the horizontal and can be coupled with the low-order normal modes of the waveguide to travel for long distances. Since these two modes are excited with relatively larger modal amplitudes compared to others, the radiated energy tends to be trapped within the waveguide by coupling with the low-order normal modes, resulting in the evident peaks observed in the frequency spectrum of $D(\theta, \phi; \omega)$.

Assuming $\theta = \phi = 0^\circ$ simplifies Eq.(32) to

$$D(0^\circ, 0^\circ; \omega) = \sum_i \lambda_i \int_S \mathbf{u}_i(y_0 + \beta) \times e^{-jk\beta} d\beta \quad (32)$$

It is now evident that when considering the radiated energy that can be coupled with low-order normal modes at small grazing angles ($\phi \approx 0^\circ$), the circumferential modes play a dominant role in the surface integral in Eq.(32). Consequently, the circumferential modes of acoustics radiation can couple with low-order normal modes of the waveguide, tending to travel to long distances. This indicates that the far-field radiation from a vibrating structure in shallow water may be simplified to the waveguide field produced by a multi-pole point source. To illustrate this, the strongest circumferential modes resulting in $D(0^\circ, 0^\circ; \omega)$ are displayed at 27 Hz, 39 Hz, 68 Hz, 81 Hz, 99 Hz, 107 Hz, 121 Hz, and 145 Hz (where peaks occur) on the right side of Fig.10.

4.3. Computational complexity

In this section, the computational efficiency of the proposed analytical solution is discussed by comparing it with the coupled FEM/WSM solver. Assuming the same number of field points to be predicted, the operation number of the FEM/WSM method is $O(MN)$, where M and N represent the numbers of equivalent sources and normal modes, respectively. For the proposed analytical solution, which only involves a one-time computation of the summation of normal modes, the computational complexity is only $O(N)$. In WSM, M is approximately of $O(k_0^2 S_a)$, where k_0 is the reference wavenumber and S_a is the surface area (Lee et al., 2011). Considering an ideal waveguide with a rigid bottom and isovelocity water, the number of normal modes N is $h\omega/(\pi c) + 1/2$. It is noteworthy that the number of modes supported in an ideal waveguide is generally significantly higher than that in a realistic waveguide with an absorbing bottom. Typically, $M \gg N$ is applied to low-frequency detection in shallow water because the surface area of the structure S_a is more than one order of magnitude larger than the water depth h .

A comparison of computational complexity is shown in Fig.12; the operation number of the two models as a function of frequency is plotted, with a water depth $h=200$ m. The computational cost of the coupled FEM/WSM

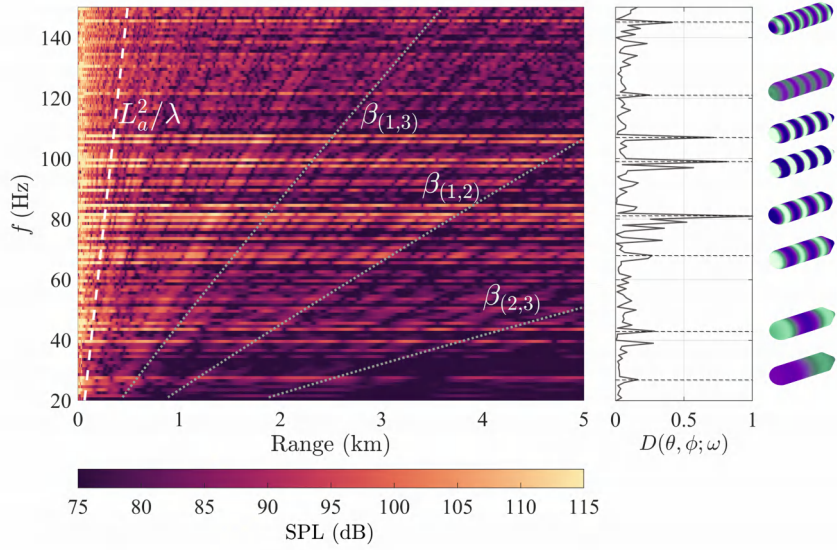


Figure 10: The left panel shows the range-frequency spectrogram of the radiation field. The white dashed line indicates the location of L_a^2/λ and the gray dashed lines represent the interference fringes with slopes of $\beta_{(1,2)}$, $\beta_{(1,3)}$ and $\beta_{(2,3)}$. The middle panel shows the normalized directional function $D(\theta, \phi; \omega)$, with the azimuth angle $\theta = 0^\circ$ and the grazing angle $\phi = 0^\circ$. The right panel illustrates the strongest radiation mode corresponding to the peak frequencies in $D(0^\circ, 0^\circ; \omega)$.

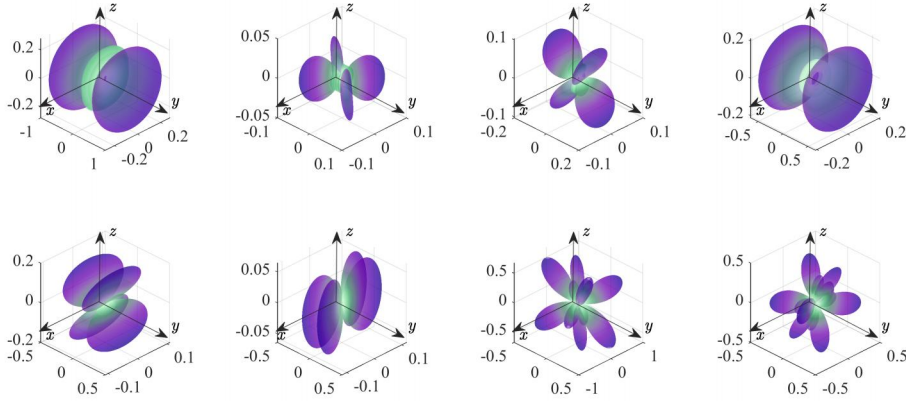


Figure 11: The normalized directionality $D_i^{\text{norm}}(\theta, \phi; \omega)$ of the first eight acoustic radiation modes at frequency $f=81\text{Hz}$.

solver increases significantly with increasing frequency, depending on $M \times N$. Nevertheless, the proposed analytical solution only requires $O(N)$ operations to predict the far-field radiation, thereby reducing the computational cost. Note that the proposed analytical solution outperforms the coupled FEM/WSM solver in terms of computational complexity by saving $O(M)$ operations. This represents a significant improvement in computational efficiency at high frequencies.

Next, a comparison of the running times is presented. The same elastic sphere and Pekeris waveguide in Section 4.1 were used in this case. The mesh sizes of the predicted field points were set to $\Delta z = 0.25$ m, $\Delta r = 2.5$ m, and $\Delta \theta = 1^\circ$. All computations were performed on a PC equipped with an Intel(R) i7-12700F 3.60 GHz processor and 32 GB of memory. The computational program was compiled using MATLAB 2022a, running in parallel to accelerate the WSM solver. The 'parfor' function in MATLAB was used to save time in repeatedly calculating the acoustic field of each equivalent source. This approach allows us to distribute the computations across multiple CPU cores to

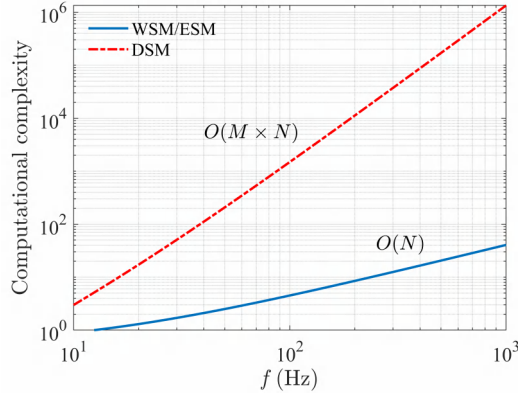


Figure 12: Comparison of computational complexity between the two methods.

Table 1

Runtime test comparison between WSM and DSM.

$r(\text{km})$	0 – 10				0 – 1	0 – 5	0 – 10	0 – 50
$f(\text{Hz})$	75	100	125	150	75			
$t_{\text{WSM}}(s)$	1080.032	1530.935	2040.860	5193.558	2596.779	563.392	1080.032	5388.374
$t_{\text{DSM}}(s)$	6.947	7.548	8.225	8.475	1.792	3.068	6.947	22.670

improve performance, with twelve processes used here for parallel computation. Table 1 presents a comparison of the computational times. The results exclude the calculation time of the FEM.

It can be seen that the running time of the WSM increases dramatically as the frequency increases when predicting the radiation on mesh ranging from 0 to 10 km, reaching up to 5193 s at 150 Hz. By contrast, the proposed analytical solution completed the computation within a few seconds. In addition, the running time of the analytical solution barely changed across the 75–150 Hz frequency range. The high efficiency achieved by the analytical solution is owing to the avoidance of repetitive computations for different equivalent sources. Again, the time comparison at 75 Hz for predictions with different ranges confirmed the high efficiency achieved by the analytical solution. Therefore, the proposed analytical solution is preferable for solving large-scale three-dimensional (3D) acoustic radiation from structures in shallow water, which represents a significant improvement in calculation efficiency because only a few seconds are required for long-range predictions.

4.4. Critical distance distinguishing the near-field and far-field radiation

In this section, we analyze the critical distance that distinguishes near- and far-field structural acoustic radiation in shallow water, and discuss the influence of the environment and radiator parameters. A depth-averaged error was introduced to identify the near-field region in which the approximation made for the proposed analytical solution is violated. These errors are defined as follows:

$$\text{Err}(r) = 20 \log_{10} \left| \frac{\sum_i^{N_z} |p_{\text{WSM}}(r, z_i)| - \sum_i^{N_z} |p_{\text{DSM}}(r, z_i)|}{N_z} \right| \quad (33)$$

where $p_{\text{WSM}}(r, z_j)$ and $p_{\text{DSM}}(r, z_j)$ denote the sound pressures calculated by the coupled FEM/WSM solver and the proposed analytical solution in the depth-range plane, respectively; z_j is the depth of the j th receiver; and N_z denotes the number of receivers across different depths.

According to Eq.(29), the critical distance r_d is determined by the wave number k_0 and L_a . L_a depends on the type of excitation, frequency, and the geometric and material properties of the structure. The far-field approximation assumes that L_a is the maximum length of the structure, meaning that each patch on the surface of the structure emits

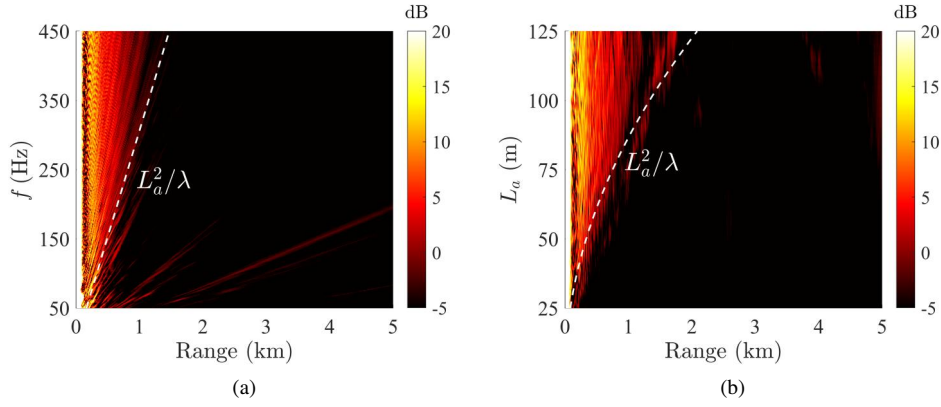


Figure 13: (a) Depth-averaged error (dB) in different frequency f with water depth $h=200$ m and $L_a=70$ m. (b) Depth-averaged error (dB) in different frequencies L_a at water depth $h=200$ m and frequency $f=200$ Hz. White dashed lines in (a) and (b) represent L_a^2/λ , indicating the critical distance.

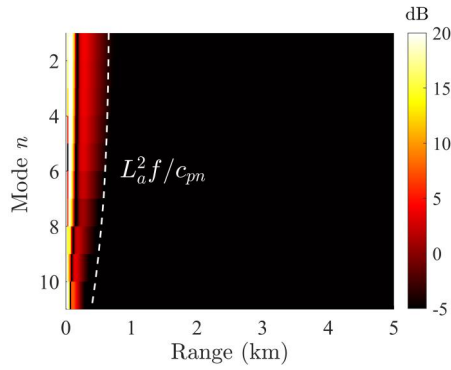


Figure 14: Depth-averaged error (dB) in different modes n with frequency $f=100$ Hz, water depth $h=200$ m, and $L_a=70$ m. The white dashed line means the $L_a^2 f / c_{pn}$, and indicates the critical distance for mode n .

radiation. In reality, only local patches of a vibrating elastic structure generate acoustic radiation. Therefore, L_a is typically smaller than the maximum length of the structure.

In this case, a finite-length line source was used to simulate the volume radiator. A uniform normal velocity distribution was imposed along the line source, and the intensity of each equivalent source q_m was equal to 1 Pa·m. The hull was placed at half the water depth, that is $z_s=h/2$, and the seabed parameters were the same as those in Section 4.1.

Fig.13 plots the errors determined by the range and the frequency and those by the range and the effective size of the radiator, respectively. The critical distance L_a^2/λ is indicated by the white dashed line. The length of the line structure L_a is 70 m, as shown in Fig.13(a), and the frequency f is 200 Hz in Fig.13(b), respectively. Clear transitioning behavior can be observed in the error distribution, accurately distinguishing the near- and far-field radiation by the critical distance indicated by the white line. Errors up to 20 dB occurred in the near-field region, where the proposed analytical solution was invalid. However, in the far-field region, the errors of the analytical solution barely exceeded -5 dB. Interestingly, oblique fringes with a concentrated error distribution were observed in the far-field region, as shown in Fig.13(a), which are associated with the interference pattern between different normal modes. This pattern can be approximated using β , which predicts the position at the trough of the waveguide field. According to the analysis presented in Section 4.2.3, large errors in the analytical solution were associated with the trough of the sound field, which explains the observed oblique fringes.

Next, we analyze the errors compared with the results of the coupled FEM/WSM by accounting for the individual modes in Eq.(33). Unlike in free space, the Fraunhofer far-field approximation in shallow water depends on the

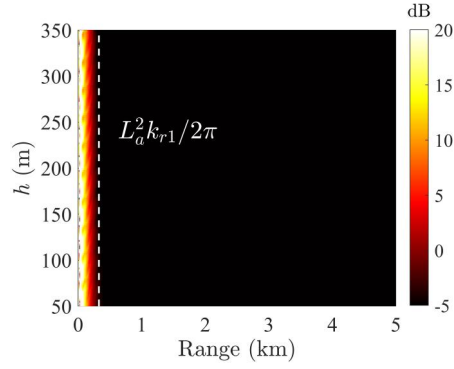


Figure 15: Depth-averaged error (dB) in different water depth h with frequency $f=100$ Hz and $L_a=70$ m. The white dashed line indicates the $L_a^2 k_{r1}/2\pi$.

horizontal wave numbers corresponding to different normal modes rather than the acoustic wave number. Fig.14 illustrates the error distribution over mode number at 100 Hz. The hull model presented in Section 4.2.2 was used. The error distribution exhibits an evident increasing trend as the mode number decreases in the transitioning region, which coincides with the white dashed line predicted by $L_a^2 f/c_{pn}$, where c_{pn} represents the modal phase velocities. This confirms that the applicability of the Fraunhofer far-field approximation in shallow water relies on the horizontal wavenumber, which increases as the mode order decreases.

It is necessary to analyze the influence of the water depth on the validity of the far-field approximation because the horizontal wave number varies with the water depth. Fig.15 plots the error distribution determined by the range and the water depth in a Pekeris waveguide with the sediment parameters given in Section 4.2.1. Unexpectedly, although the horizontal wavenumber depends directly on h , the transition distance barely changes with varying water depth. The underlying reason is that changes in h contribute relatively little to the horizontal wavenumber. To illustrate this, we introduce the equivalent depth approximation of (Buckingham and Giddens, 2006)

$$k_{rn} \approx \pm \sqrt{k_0^2 - n^2 \pi^2 / h^2} \mp \frac{i \gamma_b n^2 \pi^2 \cot^2(\alpha_b)}{\sigma_b k_0^2 h^3 \sin(\alpha_b)} \quad (34)$$

where $\alpha_b = \cos^{-1}(k_0/k_b)$ is the critical grazing angle at the bottom, $\sigma_b = \rho/\rho_b$ is the density ratio, and γ_b is the tangent wavenumber of plane waves propagating through the sediment. The term $\gamma_b \cot^2(\alpha_b)/(\sigma_b \sin(\alpha_b))$ reflects the influence of the seabed parameter on horizontal wave numbers. When considering the critical distance r_d , we reduce the imaginary part of the equivalent depth approximation, that is, k_{rn} is negligible. As a result, the imaginary part in the equivalent depth approximation can be reduced, leading to the simplification,

$$k_{rn} \approx \sqrt{k_0^2 - n^2 \pi^2 / h^2} \quad (35)$$

This simplification reveals that the change in water depth is at least two orders of magnitude smaller than that of k_{r1} , and hence the associated effects on k_{r1} are small, if not negligible. Similarly, seafloor parameters have a negligible impact on k_{rn} . This suggests that the frequency and radiator size are the predominant contributors to determining where the critical distance is imposed, instead of the waveguide environment parameters such as water depth and seabed properties.

5. Conclusion

This paper presents an efficient hybrid method for solving the problem of acoustic radiation from a vibrating structure in shallow water. In this method, the structural vibration is solved using the FEM, whereas the near-field acoustic radiation is solved using the WSM with Green's function computed using the normal mode theory. Instead of numerically calculating the integral representing the Helmholtz exterior problem, which has been reported in the literature, we derived an analytical solution for the source-strength integral of the waveguide Green's function. This

represents a significant improvement in terms of computational efficiency, allowing for onboard, real-time prediction of structural radiation in shallow water within seconds.

The proposed method was validated against a 2D axisymmetric FEM model benchmark case, in which an elastic sphere excited by an on-axis force was analyzed in the Pekeris waveguide. By further extending the simulations to consider a more realistic shell model and shallow water with SSPs, the errors of the proposed analytical solution were studied. These errors are associated with the trough of the waveguide field and the region where the far-field approximation is violated. The critical distance identifying the near and far fields of structural acoustic radiation was investigated, and it was found that this distance is dominated by the frequency and radiator size rather than the environmental parameters of the waveguide.

Furthermore, the coupling mechanism between the acoustic radiation modes and the propagation modes was investigated by simulating the LOFAR spectrum of the mechanical vibration noise using the proposed method. Two types of fringe patterns are observed in the spectrum. The oblique pattern results from the interference between different normal modes, coinciding with waveguide invariant β . On the other hand, the stronger, horizontal fringe was caused by the strong excitation of the circumferential radiation modes, independent of the waveguide parameters. This suggests that the circumferential radiation modes can couple with low-order normal modes, and tend to travel long-range at low grazing angles relative to the horizontal. This also means that in the far field, the structural radiation degenerates to the radiated field produced by a multipole point source, as only low-order normal modes coupled with the energy from the circumferential modes can propagate to the far field. This information will be valuable for detection of passive sonar operating in shallow water.

However, the added mass effect from the upper and lower boundaries on fluid loading is neglected, as the structure is assumed to be sufficiently removed from both the sea surface and the seabed. The interference between different radiation modes increase errors in regions close to the troughs of the radiation field. While this study focuses the radiation field in range-independent environments, our future work will extend the models to account for radiated sound fields in range-dependent environments, considering fluctuating interfaces and turbulent sound speeds.

Acknowledgments

This work was supported by the National Natural Science Foundation of China (Grant No. 12374423 and Grant No. 12304499) and the Stable Supporting Fund of the National Key Laboratory of Underwater Acoustic Technology (Grant No. JCKYS2023604 SSJS018).

CRedit authorship contribution statement

Ruixin Nie: Conceptualization, Methodology, Software, Validation, Writing – original draft. **Tengjiao He:** Conceptualization, Methodology, Investigation, Writing — review and editing. **Jun Fan:** Conceptualization, Formal analysis, Supervision. **Kaiqi Zhao:** Conceptualization, Supervision. **Bin Wang:** Conceptualization, Supervision, Writing – review and editing, Project administration.

References

- Bi, W., Pagneux, V., Lafarge, D., Aurégan, Y., 2007. An improved multimodal method for sound propagation in nonuniform lined ducts. *The Journal of the Acoustical Society of America* 122, 280–290. URL: <https://doi.org/10.1121/1.2736785>, doi:10.1121/1.2736785, arXiv:https://pubs.aip.org/asa/jasa/article-pdf/122/1/280/16723403/280_1_online.pdf.
- Borgiotti, G.V., 1990. The power radiated by a vibrating body in an acoustic fluid and its determination from boundary measurements. *The Journal of the Acoustical Society of America* 88, 1884–1893.
- Brunner, D., Of, G., Junge, M., Steinbach, O., Gaul, L., 2010. A fast be-fe coupling scheme for partly immersed bodies. *International Journal for Numerical Methods in Engineering* 81, 28–47. URL: <https://onlinelibrary.wiley.com/doi/abs/10.1002/nme.2672>, doi:<https://doi.org/10.1002/nme.2672>, arXiv:<https://onlinelibrary.wiley.com/doi/pdf/10.1002/nme.2672>.
- Buckingham, M.J., Giddens, E.M., 2006. Theory of sound propagation from a moving source in a three-layer Pekeris waveguide. *The Journal of the Acoustical Society of America* 120, 1825–1841. URL: <https://doi.org/10.1121/1.2258095>, doi:10.1121/1.2258095, arXiv:https://pubs.aip.org/asa/jasa/article-pdf/120/4/1825/15279554/1825_1_online.pdf.
- Chen, L., Lian, H., Pei, Q., Meng, Z., Jiang, S., Dong, H.W., Yu, P., 2024. Fem-bem analysis of acoustic interaction with submerged thin-shell structures under seabed reflection conditions. *Ocean Engineering* 309, 118554. URL: <https://www.sciencedirect.com/science/article/pii/S0029801824018924>, doi:<https://doi.org/10.1016/j.oceaneng.2024.118554>.
- Chuprov, S., Brekhovskikh, L., 1982. Interference structure of a sound field in a layered ocean. *Ocean Acoustics, Current State*, 71–91.

- Freund, J.B., Lele, S.K., Moin, P., 1996. Calculation of the radiated sound field using an open kirchhoff surface. *AIAA Journal* 34, 909–916. URL: <https://doi.org/10.2514/3.13167>, doi:10.2514/3.13167, arXiv:<https://doi.org/10.2514/3.13167>.
- Goodman, J.W., 2005. Introduction to Fourier optics. Roberts and Company publishers.
- Guo, W., Li, T., Zhu, X., Miao, Y., Zhang, G., 2017. Vibration and acoustic radiation of a finite cylindrical shell submerged at finite depth from the free surface. *Journal of Sound and Vibration* 393, 338–352. URL: <https://www.sciencedirect.com/science/article/pii/S0022460X17300044>, doi:<https://doi.org/10.1016/j.jsv.2017.01.003>.
- Haug, A.J., Graves, R.D., Überall, H., 1975. Normal-mode theory of underwater sound propagation from stationary multipole sources: results for a realistic sound-speed profile. *The Journal of the Acoustical Society of America* 57, 1052–1061. URL: <https://doi.org/10.1121/1.380553>, doi:10.1121/1.380553, arXiv:https://pubs.aip.org/asa/jasa/article-pdf/57/5/1052/11865340/1052_1_online.pdf.
- He, T., Liu, J., Ye, S., Qing, X., Mo, S., 2024. A novel model order reduction technique for solving horizontal refraction equations in the modeling of three-dimensional underwater acoustic propagation. *Journal of Sound and Vibration* 591, 118617. URL: <https://www.sciencedirect.com/science/article/pii/S0022460X24003791>, doi:<https://doi.org/10.1016/j.jsv.2024.118617>.
- He, T., Mo, S., Guo, W., Fang, E., 2021. Modeling propagation in shallow water with the range-dependent sea surfaces and fluid seabeds using the equivalent source method. *The Journal of the Acoustical Society of America* 149, 997–1011. URL: <https://doi.org/10.1121/10.0003385>, doi:10.1121/10.0003385, arXiv:https://pubs.aip.org/asa/jasa/article-pdf/149/2/997/15348890/997_1_online.pdf.
- He, T., Wang, B., Mo, S., Fang, E., 2023. Predicting range-dependent underwater sound propagation from structural sources in shallow water using coupled finite element/equivalent source computations. *Ocean Engineering* 272, 113904. URL: <https://www.sciencedirect.com/science/article/pii/S0029801823002883>, doi:<https://doi.org/10.1016/j.oceaneng.2023.113904>.
- Huang, H., Zou, M.S., Jiang, L.W., 2019. Study on the integrated calculation method of fluid–structure interaction vibration, acoustic radiation, and propagation from an elastic spherical shell in ocean acoustic environments. *Ocean Engineering* 177, 29–39. URL: <https://www.sciencedirect.com/science/article/pii/S0029801818310254>, doi:<https://doi.org/10.1016/j.oceaneng.2019.02.032>.
- Isakson, M.J., Chotiros, N.P., 2011. Finite element modeling of reverberation and transmission loss in shallow water waveguides with rough boundaries. *The Journal of the Acoustical Society of America* 129, 1273–1279. URL: <https://doi.org/10.1121/1.3531810>, doi:10.1121/1.3531810, arXiv:https://pubs.aip.org/asa/jasa/article-pdf/129/3/1273/15294581/1273_1_online.pdf.
- Jensen, F.B., Kuperman, W.A., Porter, M.B., Schmidt, H., McKay, S., 1995. Computational Ocean Acoustics. *Computer in Physics* 9, 55–56. URL: <https://doi.org/10.1063/1.4823373>, doi:10.1063/1.4823373, arXiv:https://pubs.aip.org/aip/cip/article-pdf/9/1/55/7865780/55_6_online.pdf.
- Jiang, L., Zou, M., Huang, H., Feng, X., 2018. Integrated calculation method of acoustic radiation and propagation for floating bodies in shallow water. *The Journal of the Acoustical Society of America* 143, EL430–EL436. URL: <https://doi.org/10.1121/1.5039415>, doi:10.1121/1.5039415, arXiv:https://pubs.aip.org/asa/jasa/article-pdf/143/5/EL430/13879388/el430_1_online.pdf.
- Jin, G., Ma, X., Wang, W., Liu, Z., 2018. An energy-based formulation for vibro-acoustic analysis of submerged submarine hull structures. *Ocean Engineering* 164, 402–413. URL: <https://www.sciencedirect.com/science/article/pii/S0029801818311387>, doi:<https://doi.org/10.1016/j.oceaneng.2018.06.057>.
- Kha, J., Karimi, M., Maxit, L., Kirby, R., 2024. Near- and far-field radiated acoustic pressures from a vibrating three-dimensional cylindrical shell in an underwater acoustic waveguide. *Journal of Sound and Vibration* 590, 118534. URL: <https://www.sciencedirect.com/science/article/pii/S0022460X24002979>, doi:<https://doi.org/10.1016/j.jsv.2024.118534>.
- Kha, J., Karimi, M., Maxit, L., Skvortsov, A., Kirby, R., 2023. Forced vibroacoustic response of a cylindrical shell in an underwater acoustic waveguide. *Ocean Engineering* 273, 113899. URL: <https://www.sciencedirect.com/science/article/pii/S0029801823002834>, doi:<https://doi.org/10.1016/j.oceaneng.2023.113899>.
- Koopmann, G.H., Song, L., Fahnlne, J.B., 1989. A method for computing acoustic fields based on the principle of wave superposition. *The Journal of the Acoustical Society of America* 86, 2433–2438. URL: <https://doi.org/10.1121/1.398450>, doi:10.1121/1.398450, arXiv:https://pubs.aip.org/asa/jasa/article-pdf/86/6/2433/11972250/2433_1_online.pdf.
- Kuznetsov, G.N., Stepanov, A.N., 2017. Approximate analytic representations of laws of attenuation in vector-scalar fields of multipole sources in a Pekeris waveguide. *Acoustical Physics* 63, 660–672. URL: <https://doi.org/10.1134/S1063771017060082>, doi:10.1134/S1063771017060082, arXiv:https://pubs.aip.org/asa/jasa/article-pdf/57/5/1052/11865340/1052_1_online.pdf.
- Lee, S., 2017. Review: The use of equivalent source method in computational acoustics. *Journal of Computational Acoustics* 25, 1630001. URL: <https://doi.org/10.1142/S0218396X16300012>, doi:10.1142/S0218396X16300012, arXiv:<https://doi.org/10.1142/S0218396X16300012>.
- Lee, S., Brentner, K.S., Morris, P.J., 2011. Assessment of time-domain equivalent source method for acoustic scattering. *AIAA journal* 49, 1897–1906.
- Li, T.Y., Miao, Y.Y., Ye, W.B., Zhu, X., Zhu, X.M., 2014. Far-field sound radiation of a submerged cylindrical shell at finite depth from the free surface. *The Journal of the Acoustical Society of America* 136, 1054–1064. URL: <https://doi.org/10.1121/1.4890638>, doi:10.1121/1.4890638, arXiv:https://pubs.aip.org/asa/jasa/article-pdf/136/3/1054/15310578/1054_1_online.pdf.
- Liu, J., Li, Q., 2021. Coupled mode sound propagation in inhomogeneous stratified waveguides. *Applied Sciences* 11. URL: <https://www.mdpi.com/2076-3417/11/9/3957>, doi:10.3390/app11093957.
- Marburg, S., Nolte, B., 2008. Computational acoustics of noise propagation in fluids: finite and boundary element methods. New York.
- Ochmann, M., 2004. The complex equivalent source method for sound propagation over an impedance plane. *The Journal of the Acoustical Society of America* 116, 3304–3311. URL: <https://doi.org/10.1121/1.1819504>, doi:10.1121/1.1819504, arXiv:https://pubs.aip.org/asa/jasa/article-pdf/116/6/3304/8094615/3304_1_online.pdf.
- Porter, M.B., 1992. The kraken normal mode program. Unknown.
- Qian, Z., Shang, D., Xu, X., He, Y., Zhai, J., 2022. A semi-analytical method for the 3d elastic structural-acoustic radiation in shallow water. *Journal of Theoretical and Computational Acoustics* 30, 2150011. URL: <https://doi.org/10.1142/S2591728521500110>, doi:10.1142/S2591728521500110, arXiv:<https://doi.org/10.1142/S2591728521500110>.

- Wang, X., Guo, W., 2016. Dynamic modeling and vibration characteristics analysis of submerged stiffened combined shells. *Ocean Engineering* 127, 226–235. URL: <https://www.sciencedirect.com/science/article/pii/S0029801816304425>, doi:<https://doi.org/10.1016/j.oceaneng.2016.10.008>.
- Williams, A. O., J., Novak, B.M., 1974. Normal-mode analysis of underwater-sound propagation with directional sources and receivers. *The Journal of the Acoustical Society of America* 55, 80–83. URL: <https://doi.org/10.1121/1.1928134>, doi:10.1121/1.1928134, arXiv:https://pubs.aip.org/asa/jasa/article-pdf/55/1/80/18781267/80_1_online.pdf.
- Wu, H., Yu, L., Jiang, W., 2019. A coupling fem/bem method with linear continuous elements for acoustic-structural interaction problems. *Applied Acoustics* 150, 44–54. URL: <https://www.sciencedirect.com/science/article/pii/S0003682X1830906X>, doi:<https://doi.org/10.1016/j.apacoust.2019.02.001>.
- Wu, H.T., Chen, P.T., 2017. Application of coupled fem/bem on the analysis of underwater radiated noise of a surface ship induced by hull vibrations. *Journal of Marine Science and Technology* 25, 21.
- Xi, Q., Fu, Z., Xue, M.A., Zou, M., Zheng, J., 2023. Analysis of underwater acoustic propagation induced by structural vibration in arctic ocean environment based on hybrid fem-wsm solver. *Ocean Engineering* 287, 115922. URL: <https://www.sciencedirect.com/science/article/pii/S0029801823023065>, doi:<https://doi.org/10.1016/j.oceaneng.2023.115922>.
- Zhang, L., xi Duan, J., long Da, L., jun Xu, G., hai Sun, X., 2020. Vibroacoustic radiation and propagation properties of slender cylindrical shell in uniform shallow sea. *Ocean Engineering* 195, 106659. URL: <https://www.sciencedirect.com/science/article/pii/S0029801819307796>, doi:<https://doi.org/10.1016/j.oceaneng.2019.106659>.
- Zhang, R., 1964. The sound field of a planar radiator. *Acta Physica Sinica* 20, 227–232. URL: <https://wulixb.iphy.ac.cn//article/id/745>, doi:10.7498/aps.20.227.
- Zhang, R., Zhu, B., 1987. Normal mode sound field of a directional radiator. *Journal of Sound and Vibration* 119, 207–213. URL: <https://www.sciencedirect.com/science/article/pii/0022460X87904494>, doi:[https://doi.org/10.1016/0022-460X\(87\)90449-4](https://doi.org/10.1016/0022-460X(87)90449-4).
- Zhao, K., Fan, J., Wang, B., Tang, W., 2020. Vibroacoustic behavior of a partially immersed cylindrical shell under point-force excitation: Analysis and experiment. *Applied Acoustics* 161, 107170. URL: <https://www.sciencedirect.com/science/article/pii/S0003682X19307352>, doi:<https://doi.org/10.1016/j.apacoust.2019.107170>.